# Utilization of Mechanically Activated Waste Red Mud as a High Performance Pseudocapacitor Electrode Material

Gourav Bhattacharya[1,2], Sam Jeffery Fishlock[1], Joy Sankar Roy[2], Anurag Pritam[2], Debosmita Banerjee[2], Sujit Deshmukh[2], Subhasis Ghosh[3], James A. McLaughlin[1*], Susanta Sinha Roy[2*]

[1]Nanotechnology and Integrated Bioengineering Centre, University of Ulster, Jordanstown Campus, Newtownabbey, BT37 0QB, Northern Ireland, UK.

[2]Department of Physics, School of Natural Sciences, Shiv Nadar University, Gautam Buddha Nagar 201314, Uttar Pradesh, India.

[3]School of Physical Sciences, Jawaharlal Nehru University, New Delhi 110067, India

E-mail: susanta.roy@snu.edu.in, jad.mclaughlin@ulster.ac.uk

## Abstract

In recent years, metal oxide based, inexpensive, stable electrodes are being explored as a potent source of high performance, sustainable supercapacitors. Here we report on the employment of industrial waste red mud as a pseudocapacitive electrode material. Mechanical alloying was used to produce uniform red mud nanoparticles which are rich in hematite ($Fe_2O_3$) and lower amounts of other metal oxides. The effect of milling time, up to 15 hours, with particle size and electrochemical stability was studied. The electrochemical measurements for the evaluation of supercapacitive properties were evaluated by using cyclic voltammetry (CV), galvanostatic charging/discharging (CD) analysis and electrochemical impedance spectroscopy (EIS). The samples with 10 hours of milling exhibited the highest stability as well as the best pseudocapacitive behaviour. A high specific capacitance of ~317 $Fg^{-1}$ was achieved at a scan rate of 10 $mVs^{-1}$ using

a 6 M aqueous KOH solution. The modified electrode showed a sp. capacitance of ~180 $Fg^{-1}$ at an elevated current density of 6 $Ag^{-1}$ with an extraordinary retention of ~97% even after 5000 cycles. A detailed quantitative electrochemical analysis was carried out to further shed light on the charge storage mechanism. The formation of uniform nanoparticles, and increased electrode stability, was correlated with the high performance of the electrode. This work presents two significant benefits for our environment in areas such as energy storage, as it allows for the production of a stable and efficient supercapacitor electrode, and in waste management with new applications for the treatment of red mud waste.

## 1. Introduction

The exploitation of non-conventional renewable energy sources is of significant worldwide interest due to the increasing global demand for energy, the rapid exhaustion of fossil fuels and other non-renewable energy resources, and environmental concerns such as global warming and climate-change [1]. Among several energy storage devices, supercapacitors, owing to their high power density, high specific capacitance and superior cyclic stability, have a huge potential as portable power storage units, and can be used efficiently in many areas such as electric vehicles, consumer electronics etc. [2-6].

The charge storage mechanism in a supercapacitor is governed either by electrical double layer capacitance (EDLC) [7, 8] or by pseudocapacitance [9, 10]. In EDLC, the charge is stored electrostatically through reversible adsorption of electrolytes onto a high surface area and electrochemically-stable electrodes. The phenomena is related to a potential-dependent accumulation of charges at the electrode-electrolyte interface [11, 12]. In pseudocapacitance, the capacitance is faradic in origin [13] whereby an ultra-fast redox reaction takes place at or near the electrode and a faradic charge is passed as a function of electrode potential [14, 15]. Carbon-based

materials such as activated carbon [16], carbon nanotubes [17], graphene [18, 19], reduced graphene oxide [20, 21] have been explored as EDLC materials whilst conducting polymers [22, 23] and transition metal oxides [24, 25] have been utilised as pseudocapacitive supercapacitor electrodes.

One of the most important factors for supercapacitor performance is the electrode material [1], and researchers across the globe are seeking inexpensive, stable and high-performance electrode materials [26, 27]. In the modern era of industrialization, a huge amount of different forms of organic and inorganic waste byproducts have been accumulating in the environment, resulting in air-water-soil pollution and an overall degradation of our ecosystems and quality of life [28-30]. Over the last decade, there is a worldwide drive towards waste management and researchers are utilising the byproducts in diverse directions for the betterment of the society [31, 32]. For example, different forms of agro-industrial organic waste have been effectively utilised for supercapacitor electrodes where biomass is converted to activated carbon [33]. A myriad of different agricultural waste types such as: cassava peel waste [34], coffee beans [35], sugarcane bagasse [36, 37] , rice husk [38, 39], sunflower seed shell [40], coffee endocarp [41], apricot shell [42], rubber wood sawdust [43], oil palm empty fruit bunch [44], argan seed shell [45], bamboo species [46] etc. are used as starting precursors for the porous activated carbon for EDLC. Chang et al. utilised waste filter papers as precursors to synthesise the activated carbon electrodes [47]. There are a few recent reports on the utilization of inorganic wastes to produce activated carbon materials. Zhi et al. used waste tires [48]. Konikkara et al. synthesised activated carbon from solid leather waste and used as an EDLC [49]. Though wastes have been utilised in EDLC supercapacitors, there is hardly any report on the waste-derived non-carbonic pseudocapacitor

electrode. Recently, Fu and coworkers produced a supercapacitor electrode based on industrial mill scale waste (iron oxide enriched) which exhibits a promising storage capability [50].

Red mud is an industrial waste which is generated during the bauxite ore processing [51]. Around 120 million tonnes of red mud and other bauxite residues are produced yearly [52] and there have been many large-scale environmental disasters involving red-mud, most recently in Hungary (2010) [53] where 10 persons were directly killed in a red mud flood, over one hundred more injured, and a large area of land and river was environmentally decimated. Thus, red mud is an abundant material which has been repeatedly shown to cause environmental horrors. This byproduct is alkaline in nature [54] and contains a rich mixture of metal oxides [55]. This waste is very common in India and after activating the red mud, researchers have to-date mainly utilised it in wastewater treatment systems such as dye degradation [56], arsenic and other heavy metal adsorption processes [57, 58]. Though it comprises more than 50% hematite ($Fe_2O_3$) which has been deployed extensively in supercapacitor electrodes, surprisingly, the potential of red mud as a pseudocapacitive material has not been explored yet.

In this report, the potential of hazardous red mud as a pseudocapacitor material has been explored. The as-received red mud from the industry was mechanically alloyed using a ball milling technique to produce uniform red mud nanoparticles. The milling time was varied as a function of particle size and electrode stability. The evaluation of electrochemical properties of mechanically activated waste nanoparticles exhibited impressive supercapacitor behaviour with a remarkable long-term stability. Furthermore, an in-depth electrochemical analysis has been undertaken to understand the origin of the storage mechanism, and hence we have established the feasibility of red mud as a promising, inexpensive electrode material.

## 2. Experimental

### 2.1. Materials

Red mud (RM) was collected from National Aluminum Company Limited (NALCO), India. The as-received powder was dehydrated for an hour at an elevated temperature (~110$^{o}$ C). The powder was further ground in an automated motor-pestle for 1 hour to produce the fine powder. All the electrolytes used herein were purchased from Fisher Scientific. All the aqueous solutions were produced with ultrapure DI water (Millipore-Q systems: electrical resistivity ~ 18 MΩ cm at room temperature (298 K).

### 2.2. Method

In order to prepare the RM nanoparticles, mechanical alloying using a planetary ball mill (Retsch, PM200) was employed. The powders were placed in a chrome steel bowl (volume ~ 60ml) filled with steel balls of diameter ~5 mm. The ball-to-powder mass ratio of 8:1 (ball: RM) was used. Milling, in the present study has been carried out at 150 rpm and was continued up to 15 hours with intermediate intervals of 1 hour.

The un-milled red mud samples will be termed as RM-0, and the ball milled particles will be termed as RM-X. Where X represents the milling time in hours. For example, the red mud nanoparticles with 10 H of milling will be represented by RM-10.

### 2.3. Characterization

#### 2.3. 1. Morphological measurements

In order to analyse the chemical composition of RM-0, X-ray fluorescence microscopy was carried out, and the elemental details have been confirmed using TEM- energy dispersive x-ray (EDX)

spectroscopy (Bruker S4 PIONEER). The morphology and particle size were monitored using Field-effect scanning electron microscopy (FESEM) and transmission electron microscopy(TEM) (JEOL 2100F). The particle size was measured using a particle size analyzer (Melvin). The crystallinity and the crystal phases were determined by X-ray diffraction technique using Bruker D8-Discover with Cu-Ka radiation (λ= 0.154 nm) The Raman spectra were recorded using a Renishaw Raman spectrometer (inVia) using a 532 nm Laser source, using nominal power of 25 mW for 60 seconds, 50 × magnification.

**2.3.2. Electrochemical measurement**

The cyclic voltammetry (CV), galvanostatic charge-discharge (CD) and electrochemical impedance spectroscopy (EIS) measurements were performed on an Autolab Potentiostat Galvanostat PGSTAT302N (Metrhom, Netherlands). For the electrochemical characterization, CV measurements were carried out in a three-electrode set-up, consisting of Ag/AgCl as the reference electrode, platinum wire as the counter electrode and glassy carbon electrode (GCE) modified with red mud particles as the working electrode. For this purpose, 5 mM of Potassium Ferro/ Ferry cyanide in 0.1 M KCl was used as the standard electrolyte. The CV scans were measured between -0.3 V to 0.7 V. In order to find out the sp. capacitance from the CV, a similar set of electrodes were utilised, and the measurements were recorded in a 6 M KOH electrolyte solution within the scan range -1.0 V to 0.2 V. The scan rates were varied, and the sp. capacitances were evaluated from the CV curve. The galvanostatic charging/discharging analysis was recorded in a chrono-potentiometry mode with the same 3-electrode set-up and similar electrolyte (6 M KOH) as used in the CV measurements. For the CD analysis, the pre-defined cut-off voltages were obtained from the CV measurements. The impedance measurements were carried out in the FRA potential scan mode with a similar electrode-electrolyte set-up where red mud coated GCE act as the working

electrode, along with platinum wire counter and Ag/AgCl reference electrode. All the measurements were carried out at room temperature. For EIS measurements, a sinusoidal alternating current (a.c.) voltage with root mean square (r.m.s.) value of 10 mV was applied as a perturbation. The frequency of the a.c. voltage was varied from 0.1 Hz to 100 kHz. The as-obtained Nyquist plots were fitted using the vendor provided NOVA software.

## 3. Results and discussions

### 3.1. Morphology analysis of RM-0

The as-obtained RM powders were at first dehydrated in an oven for 1 hour at 110°C and then ground to obtain moisture and chunk-free microparticles. The chemical components were analysed using XRF analysis and are represented in Table 1. From the table, it is quite evident that RM consists mainly of hematite and maghemite ($Fe_2O_3$) (~55%) and alumina ($Al_2O_3$). It also includes quartz ($SiO_2$), complex oxides of titanium and trace amount of various other metal oxides (magnesium, manganese, sodium etc.). In order to have a direct morphological visualization of this red mud powder, an FESEM image was taken and is shown in Fig. 1a. From the figures, it is quite evident that the RM-0 red mud particles have no uniform shape, size and particle distribution. A representative TEM image of RM-0 is shown in Fig. 1b. An EDX-TEM study of RM-0 is presented in Fig. S1. The presence of iron, aluminum, silicon, sodium, calcium, titanium, manganese is confirmed from the EDX spectra. To further confirm the crystalline phases, wide-angle X-ray diffraction analysis was carried out and is represented in Fig. 2a. The XRD patterns are similar to the previous reports [59, 60] and show the presence of crystalline hematite, maghemite, goethite, alumina, ilmenite, sodium oxide, gibbsite, calcite and silica [60, 61].

Raman spectroscopy was also carried out to probe different vibrational modes of the metal oxides present in the red mud and represented in Fig. 2b. The main peaks were attributed to the following modes: $Fe_2O_3$ hematite: $E_g$ mode at 291 and 404 $cm^{-1}$, $A_{1g}$ at 223 and 502 $cm^{-1}$ [62]; ilmenite $FeTiO_3$: $E_g^5$ mode at 146, and $A_G^1$ 662 $cm^{-1}$ [63]; $CaCO_3$ calcite: $E_g$ mode at 152 $cm^{-1}$ [64].

### 3.2. Electrochemical Characterization

#### 3.2.1. Cyclic voltammetry study

In order to find out the effect of ball milling on the red mud samples, cyclic voltammetry was carried out on a three-electrode system with red mud modified GCE electrode as the working electrode, platinum counter electrode and Ag/AgCl as a reference electrode. Fig. 3 represents CV scans of all red mud samples. CV scans were executed using a 0.1 M KCl aqueous solution containing 5 mM $Fe(CN)^{3-/4-}$ redox couple within a scan range -0.30 V to +0.70 V with a scan rate of 50 mV $s^{-1}$. For the RM-0 powder, a set of redox peaks are observed around ~0.10 V (cathodic) and ~0.56 V (anodic) with the peak anodic and cathodic current of 5.8 $Ag^{-1}$ and -5.9 $Ag^{-1}$ respectively. With increased milling time, the peak currents are found to enhance, with maximum peak currents of 59.1 $Ag^{-1}$ and ~-58.0 $Ag^{-1}$ observed in RM-10. There is a significant (~10-fold) enhancement in the peak current density which is suggestive of improved charge transfer kinetics [65] and a better electron transfer pathway in case of RM-10 sample. Different voltammetry parameters such as the anodic and cathodic peak potentials, separation potential, coulombic efficiency, and half-cell potential are calculated for all samples (RM-0 to RM-15) as represented in Table-2. The separation potential (the difference between the anodic and cathodic peak potentials) ($\Delta E_{diff}$) is a qualitative measurement of reversibility of redox reactions, where a smaller value indicates a better reversibility [66]. $\Delta E_{diff}$ was measured to be ~258 mV for RM-0 sample,

indicating the redox reaction is somewhat quasi-reversible in nature. The $\Delta E_{diff}$ for RM-3 sample was found to be ~ 313 mV implying a poor reversibility. The value is least for the RM-10 sample (~195 mV) and thus the reversibility is much improved. Further milling re-enhanced $\Delta E_{diff}$ (~305 mV for RM-15 particles).

The ratio of cathodic to anodic peak current represents the coulombic efficiency (η%) of the electrode materials. η was further evaluated from the cyclic voltammetry curve and is also tabulated in the table (Table 2). The η value for the RM-0 was found to be 96%, inferring a high charge retention of 5 mM $Fe(CN)^{3-/4-}$ redox couple in 0.1 M KCl solution. All samples exhibit efficiencies >96% with the maximum of ~98% being obtained for the RM-10 sample.

The mean of the cathodic and anodic peak potentials (half-cell potential) can be used to estimate electrochemical reversibility and the cell stability of the electrode material. The half-cell potential as a function of the milling time is shown in Table 2. From the table it is evident that there is a constant drop in the half-cell potential with milling times up to 10 hours, to a minimum of ~227 mV. Up to 10 hours of ball-milling, we observed a significant enhancement in current density, and continuous decrement in half-cell potential, and thus RM-10 samples unveiled the best electrochemical performance. After more than 10 hours of milling, the half-cell potential interestingly increased to ~231 mV for the RM-15 powder, which demonstrates a reduction in electrode stability. This is also consistent with the previous observations: i) the current density for RM-15 samples were less ii) $\Delta E_{diff}$ was higher and iii) the coulombic efficiency reduced in comparison to the RM-10 sample. In the following section, the morphological and structural changes in the red mud particles during milling will be explored and correlated to the electrochemical data.

### 3.3. Morphology analysis of ball-milled RM

The FESEM images for the ball-milled samples are shown in Supplementary Fig. S2. In general, from the Fig. S2, it is evident that the particle size tends to reduce with the increase in ball mill time. In addition to this, the particle shape changes to 'spherical like' in nature. The particle size tends to decrease with milling time up to 10 hours and then after, further reduction is seized. The TEM image for RM-10 sample is shown in Fig. 4, which showed uniform distributions of spherical, crystalline, RM nanoparticles of diameter 30-50 nm. Particle size analysis is a semi-quantitative approximation to get an estimate of the particle size distribution. In order to draw a correlation between particle size with milling time, particle size analysis was carried out and is represented in supplementary Fig. S3. From the figure, it is evident that the average particle size of RM-0 (Particle size ~210±40 nm) reduces with ball milling up to 10 hours of milling. For RM-10 sample, the average particle size was found to be ~45 ±10 nm. Interestingly, the average particle size slightly increased for RM-15 sample (diameter ~65±20 nm). It is reported earlier that longer ball-milling process introduces grain growth (due to cold-welding) and microstrains in the system and as a consequence, the particle size increased [67, 68]. Thus, the possible grain growth in RM-15 sample is responsible for the sudden reduction in current density and enhancement in half-cell potential of CV studies. RM-10 sample is found to offer the best electrochemical properties and thus will be explored further for supercapacitor application. For comparison purposes, the untreated RM-0 particles would be utilised.

### 3.4. Supercapacitor analysis

#### 3.4.1. Cyclic Voltammetry (CV)

Fig. 5 represent the Cyclic voltammetry graph for RM-0 and RM-10 particles in 6 M KOH solution at a scan rate 10 $mVs^{-1}$ using 3-electrode assembly as mentioned earlier. There is a substantial enhancement in the sp. current density (~ 16 times) and integrated area under the CV curve for RM-10 particles compared to the untreated sample. RM-10 shows a shallow broad reduction hump around ~-0.42 V which matches with the pseudocapacitance values of $Fe_2O_3$ [69]. The charge storage mechanism in case of hematite is reported to be similar to that of the magnetite [70], where the reaction and storage mechanisms are correlated with the redox reactions accompanied by the diffusion mediated intercalation [71]. Fig. 6a represents the cyclic voltammogram of RM-10 sample at different scan rates from 10 to 200 $mVs^{-1}$.

The specific capacitance of the RM 10 sample is evaluated from the CV curve by employing the following equation [72, 73]: $Cs = 0.5[I/\{(dv/dt)/m\}]$ (1)

Where, $C_s$ is the sp. capacitance, $I$ is the total current obtained from the CV curve, $dv/dt$ is the scan rate, and $m$ is the active mass of RM-10 on the glassy carbon electrode. The multiplication factor 0.5 is originated to take care of either cathodic or anodic current.

The total current $I$ can also be calculated by integrating the area of the CV curve defined as [73, 74]:

$$I = \int_{V_i}^{V_f} \frac{i(V)dV}{(V_f - V_{\mathrm{i}})} \quad (2)$$

Where, $V_i$ and $V_f$ are the lowest and highest voltage of the potential range. The specific capacitance of RM 10 as a function of scan rate is plotted in Fig. 6b. At the lowest experimental scan rate (10

mV $s^{-1}$) a sp. capacitance of ~317 $Fg^{-1}$ was obtained. At the same sweeping potential (10 mV $s^{-1}$), a sp. capacitance value of ~21 $Fg^{-1}$ was calculated for the RM-0. The poor capacitive performance of the RM-0 sample could be correlated with the non-uniform macro- RM particles with poor electrical conductivity. At the highest experimental scan rate (200 $mVs^{-1}$) a sp. capacitance of ~ 72 $Fg^{-1}$ was achieved for RM-10.

The total amount of charge stored in an electrode is governed by the contributions of both capacitive and the intercalation processes. The capacitive component consists of ion adsorption/desorption reactions at the electrode/electrolyte (double layer) and very fast faradic surface redox reactions (pseudocapacitance) [75, 76]. The appearance of these divergent energy storage mechanisms can be calculated and distinguished from the other by examining the CV scans at different scan rates according to the following power law [76, 77],

$$i = av^b \qquad (3)$$

Where, $i$ is the scan rate dependent current, $v$ is the scan rate and $a$ and $b$ are the adjustable parameters. When b is close to 1, the current is predominantly capacitive in nature, whereas b values closer to 0.5 signify the current flow at any fixed potential relates to a diffusion-controlled phenomenon [75]. Using this technique, charge storage kinetics at each potential can be mapped. To determine b values, log $i$ vs. log $v$ was plotted for different potentials and the slope of the best linear fit data provides the b value. As an example, the slope of the linear graph of log $i$ vs. log $v$ was plotted for different potentials and represented in supplementary Fig. S4. The b values for different potentials were obtained for RM-10 in 6M KOH solution and the variation of b with applied potential is plotted in Fig. 7a, which suggests that there is a large variation in the b values at different potentials. Maximum and minimum 'b' values of ~0.75 and ~0.30, respectively, were obtained which suggests that the charge storage mechanism in the RM-10 system is a combination

of both surface dependent capacitive charge storage and diffusion driven intercalation/de-intercalation phenomena [76]. In order to make out how the electrode structure offers such explicit distinctions and to differentiate the sp. capacitance contribution from the inner and outer surface of the electrode, Trasatti's method [76, 78, 79] was employed.

The basic method originates from the postulation that the surface and diffusion-controlled storage mechanisms are manifested by different kinetic models and have different responses towards the sweeping rate [78]. When the scan rate is high, the charge is stored only at the easily accessible outer surface because of the slower diffusion of electrolyte ion to the inner surface of RM-10. Thus, the contributions from the subsurface regions can be excluded. On the other hand, at relatively low scan rate the ions can diffuse through and the total charge stored is an additive effect of both the inner and outer surface of the RM-10 modified glassy carbon electrode. Fig. 7b exhibits a plot of $1/C_s$ for RM-10 as a function of square root of sweeping rate ($v$) within 10-100 mV $s^{-1}$. In this region, the contribution of both surface and diffusion-driven storage mechanisms are prominent [76]. The sp. capacitance at very slow scan rates was estimated from the intercept of the best fit linear plot with the $1/C_s$ axis [78]. The total sp. capacitance of ~417 $Fg^{-1}$ was obtained. In order to extract the surface-governed capacitance, the specific capacitance ($C_s$) graph was plotted as a function of $v^{-1/2}$ and represented in Fig. 7c. Here the linear region intercepts of the plot with the $C_s$ predicted the surface governed capacitance at higher scan rate as ~76 $Fg^{-1}$. After calculation, the results predict that the ~82% of the total sp. capacitance arises from the diffusion-controlled processes and the residual capacitance of ~ 18% is surface governed. Thus the charge storage mechanism is dominated by diffusion controlled pseudocapacitance [14]. The presence of only pseudocapacitive metal oxides in RM and absence of any porous carbon-based (higher surface area) material, limits the surface capacitance [77] and as the RM-10 modified GCE electrode stores

more charges in the inner surface due to the low ionic solvation radius [80] and high ionic mobility of the electrolyte [80]. The presence of surface adsorbed solvent molecules (water), which could enhance the accessibility of ions into electrodes, may facilitate the improved ionic diffusivity [81].

### 3.4.2. Galvanostatic Charging/Discharging Analysis

To determine the sp. capacitance and cyclic stability, the RM-10 modified GCE was galvanostatically charged/discharged within the same potential range as in the CV scan (-1.0 to 0.2 V vs. Ag/AgCl reference electrode), in the same 6M KOH electrolyte. The specific capacitance values for RM-10 nanoparticles from the galvanostatic charging/discharging analysis were evaluated from the following equation [72]

$$C_s = -[i/\{(dv/dt)m\}] \qquad (4)$$

Where $C_s$ is the gravimetric sp. capacitance, $m$ is the active mass of the electrode and $dv/dt$ is the average slope of the discharge cycle. The quasi-symmetric charging-discharging cycles in Fig. 8a delineate a stable electrode performance [82] whereas the curvature in the plot during discharge illustrates the presence of pseudocapacitance [72, 83] which has already been discussed in the earlier section.

The charging/discharging plot (at a sp. current density of 6 $Ag^{-1}$) for RM-0 and RM-10 nanoparticles are represented in supplementary Fig. S5. The charge-discharge period in case of RM-10 is higher than RM-0 which also indicates a higher charge storage capability [72]. The sp. capacitance was further calculated using equation (4). The specific capacitance for the RM-10 sample is ~ 180 $Fg^{-1}$, compared with ~24 $Fg^{-1}$ for RM-0. The non-uniform morphology and poor current density of RM-0 are responsible for the poor capacitance in this sample. The ball milled sample (RM-10) demonstrated a much-improved electron transfer kinetics in the CV scan possibly

due to two factors first, uniform morphology with smaller particle size, secondly, due to enhanced ion diffusion into the inner surfaces of the electrode.

The gravimetric capacitance was calculated from the charging-discharging graphs for different sp. current densities and represented in Fig. 8a. The sp. capacitance as a function of sp. current density was plotted in Fig. 8b. The maximum capacitance of ~ 280 $Fg^{-1}$ was achieved at a current density of 1 $Ag^{-1}$, whereas at an extremely high sp. current density of 20 $Ag^{-1}$, a moderate capacitance of 80 $Fg^{-1}$ was obtained. The retention of a steady capacitance even in such ultra-high sp. current density emphasises the stability of the RM-10 modified GCE and reinforces its suitability as a supercapacitor electrode material [84, 85].

Long-term cyclic stability is one of the key parameters to determine the performance of any supercapacitor material [86]. Hence, to probe the long-term cyclic stability, the charging/discharging measurement was carried out for 5000 cycles using a relatively high sp. current density of 6 $Ag^{-1}$. The sp. capacitance as a function of cycle number is plotted in Fig. 8c. The system shows a remarkable capacitance retention and even after 5000 cycles, ~97% capacitance was still retained (inset of Fig. 8c). Particle agglomeration, material degradation and leaching during charging/discharging are the prime causes of losses in capacitance [87]. Here, the RM nanoparticles obtained by the ball-milling process (RM-10) are stable, and the morphological uniformity and the presence of other metal oxides (especially goethite) apart from iron oxide may slow down the agglomeration process [88, 89]. In addition to this, there was hardly any material leaching in the electrolyte solution during charging/discharging which could also hinder the charge loss [90].

Charging/discharging coulombic efficiency ( $\eta_{cd}$) is another important parameter and which could also provide significant information about long-term stability and charge-storage mechanism. $\eta_{cd}$ is calculated using the following relation [85, 91]:

$$\eta_{cd} = \frac{charging\ time}{discharging\ time}\ x\ 100\% \qquad (5)$$

The charging/discharging coulombic efficiency is calculated and $\eta_{cd}$ was found to be ~ 150%. Coulombic efficiencies with similar results (greater than 100%) have been reported in the literature [91]; physically it means that the system can be charged rapidly and discharged at a relatively slow rate, which suggests RM-10 may be utilised as a promising hybrid battery-type supercapacitor [91]. The variation in $\eta_{cd}$ during cyclic test was also monitored and a 98% retention in $\eta_{cd}$ value was achieved after 5000 cycles, which indicates an excellent reversibility of RM-10 modified GCE during charge/discharge process [90].

Ragone plots [92] are often used to express power densities and energy densities of a supercapacitor and represented in Fig. 9 for the RM-10 sample. The sp. energy density $E_s$ (Wh $kg^{-1}$) was calculated as [72]:

$$E_s = 0.5 C_s V^2 \qquad (6)$$

Where, $C_s$ is the sp. capacitance obtained from CD and $V$ is the effective potential window. The sp. power density $P_s$ (W $kg^{-1}$) was calculated using the following equation:

$$P_s = {}^{E_s}/_{t_d} \qquad (7)$$

Where, $E_s$ is the sp. energy density and $t_d$ is the discharge time.

Performance of the RM-10 electrodes are compared with other metal oxide-based supercapacitors in terms of energy density (Wh $kg^{-1}$) and power density (kW $kg^{-1}$) in a Ragone plot (Fig. 9). The comparative plot shows that the RM-10 nanoparticles exhibit better performance as compared to iron oxide rich industrial mill scale waste ($FeO_x$) [50], composite metal oxides (AC/FCO) electrode [93] and a two-electrode supercapacitor comprised of ruthenium oxide nanoparticles [94].

The highest energy density was measured as 56 Wh $kg^{-1}$ at a sp. current density of 1 $Ag^{-1}$ and a maximum power density of 12 kW $kg^{-1}$ at a higher current density of 20 $Ag^{-1}$. Even at this higher current density, the sp. energy density was evaluated as ~16 Wh $kg^{-1}$ indicating a better stability of the electrode even at high current density.

3.4.3. **Electrochemical impedance spectroscopy (EIS) study**

In order to understand the ionic diffusion and charge transfer kinetics of the RM electrodes, electrochemical impedance spectroscopy (EIS) technique has been employed. EIS is a non-destructive, fast and simple technique to excerpt the electrode kinetics of the test material [95]. Here the real part of impedance is plotted against the imaginary part (Nyquist plot). In this study, a perturbation voltage with an r.m.s. value of 10 mV was applied while the frequency was varied from 0.1–100 kHz. The Nyquist plots of RM-0 and RM-10 particles are represented in Fig. 10a. The plot can be categorised in two separate regions. A semicircular nature was observed in the high frequency region and it had a protracted tail in lower frequency regimes. The linear tail originates from the frequency-dependent ion transport and/or diffusion of ions at outer and inner surfaces of the electrode [96]. The magnitude of the series resistance is slightly decreased after the ball milling process (for clarity, the region is magnified in the inset of Fig. 10a). The diameter of the semicircle of the Nyquist plot determines the charge transport resistance of a system [97]. The

decrease in the diameter of the RM-10 sample favours diffusion of the electrolyte in the electrode surface.

The EIS data was further modelled and fitted using a model equivalent electrical circuit (Fig. 10b). The equivalent circuit consists of a series resistance, a charge transfer resistance and two constant phase elements (CPE) as described by Fu et al. [50] and Bisquertet et al. [98]. The series resistance takes care of the cumulative effects of sum of contact resistance, material resistance and electrolyte resistance [77]. The CPE (Z) is defined as $Z = Y_0(j\omega)^{-\alpha}$, where $Y_0$= 1/C for $\alpha$ = 1 and, $Y_0$= R for $\alpha$ = 0; C and R represents the capacitance and resistance respectively. $\alpha$ is the exponent of CPE. When $\alpha$ = 0, this represents a purely resistive element whereas $\alpha$ =1 means the component is purely capacitive in nature [99]. The first CPE represents the conventional double layer and redox capacitance along with the non-linearity and the second one represents the CPE at low-frequency region which appears due to the roughness at the blocking interface [98], non-linearity and diffusion driven intercalation.

The fitted curves for RM-0 and RM-10 samples showed residual $\chi^2$ values of ~0.001 and ~0.002 respectively confirming an excellent fitting. The values obtained from the equivalent circuit fitting were also tabulated in Table 3. The charge transfer resistance for RM-0 was evaluated as ~17 Ω, which reduced to ~11 Ω in RM-10 sample. The series resistance was also reduced to ~3 Ω from ~9 Ω in case of RM-10 sample. The minimal equivalent series resistance and charge transfer resistance of RM-10 sample can be related to its smaller size and highly-ordered and uniform morphology which contributes to an advantageous intrinsic electronic conductivity [100]. The minimal charge transfer resistance also indicates a high diffusion of electrolytes. The constant phase element in the equivalent circuit for RM samples also verifies the presence of both capacitive

and diffusion governed charge storage (intercalation) process which again proves the complex charge storage mechanism and diffusion dominated pseudocapacitance.

## 4. Conclusion

The present work successfully validated the suitability of mechanically activated red mud as a potent source of energy storage material. Mechanical alloying by ball milling offers uniform morphology and higher charge transfer kinetics, from this industrial waste material. In-depth electrochemical performance assessment showed that the RM-10 modified GCE exhibited high sp. capacitance, high energy density and power density with a remarkable long-term cyclic stability. The storage mechanism was found to be diffusion-dominated in nature. The calculated coulombic efficiency also confirmed the battery-like pseudocapacitance of ball-milled RM-10 sample. Importantly, the present approach to producing a high-performance supercapacitor electrode material from industrial waste is green, inexpensive and sustainable. The method also deals with an alternative path towards waste management and sustainability. In future, the performance could further be improved by producing hybrid supercapacitors using mechanically treated waste red mud.

## Acknowledgement

Gourav Bhattacharya is a Commonwealth Scholar (Split-Site Scholarship), funded by the UK Government. GB, SF and JM Acknowledge the financial support from the Biodevices Laboratory and Invest Northern Ireland. Anurag Pritam, Debosmita Banerjee and Sujit Deshmukh are indebted to Shiv Nadar University for providing PhD scholarships.

**References**

[1] Wang G, Zhang L, Zhang J. A review of electrode materials for electrochemical supercapacitors. Chemical Society Reviews. 2012;41:797-828.

[2] Simon P, Gogotsi Y. Materials for electrochemical capacitors. Nature materials. 2008;7:845.

[3] Wei TY, Chen CH, Chien HC, Lu SY, Hu CC. A cost-effective supercapacitor material of ultrahigh specific capacitances: spinel nickel cobaltite aerogels from an epoxide-driven sol–gel process. Advanced materials. 2010;22:347-51.

[4] El-Kady MF, Kaner RB. Scalable fabrication of high-power graphene micro-supercapacitors for flexible and on-chip energy storage. Nature communications. 2013;4:ncomms2446.

[5] Yu X, Lu B, Xu Z. Super long-life supercapacitors based on the construction of nanohoneycomb-like strongly coupled $CoMoO_4$–3D graphene hybrid electrodes. Advanced materials. 2014;26:1044-51.

[6] Snook GA, Kao P, Best AS. Conducting-polymer-based supercapacitor devices and electrodes. Journal of Power Sources. 2011;196:1-12.

[7] Sharma P, Bhatti T. A review on electrochemical double-layer capacitors. Energy conversion and management. 2010;51:2901-12.

[8] Zhang Y, Feng H, Wu X, Wang L, Zhang A, Xia T, et al. Progress of electrochemical capacitor electrode materials: A review. International journal of hydrogen energy. 2009;34:4889-99.

[9] Wang H, Casalongue HS, Liang Y, Dai H. $Ni(OH)_2$ nanoplates grown on graphene as advanced electrochemical pseudocapacitor materials. Journal of the American Chemical Society. 2010;132:7472-7.

[10] Hercule KM, Wei Q, Khan AM, Zhao Y, Tian X, Mai L. Synergistic effect of hierarchical nanostructured $MoO_2$/$Co(OH)_2$ with largely enhanced pseudocapacitor cyclability. Nano letters. 2013;13:5685-91.

[11] Simon P, Gogotsi Y. Charge storage mechanism in nanoporous carbons and its consequence for electrical double layer capacitors. Philosophical Transactions of the Royal Society of London A: Mathematical, Physical and Engineering Sciences. 2010;368:3457-67.

[12] Conway B. Theory and principles of electrode processesRonald Press. London; 1965.

[13] Toupin M, Brousse T, Bélanger D. Charge storage mechanism of $MnO_2$ electrode used in aqueous electrochemical capacitor. Chemistry of Materials. 2004;16:3184-90.

[14] Conway B, Pell W. Double-layer and pseudocapacitance types of electrochemical capacitors and their applications to the development of hybrid devices. Journal of Solid State Electrochemistry. 2003;7:637-44.

[15] Kuo S-L, Lee J-F, Wu N-L. Study on pseudocapacitance mechanism of aqueous $MnFe_2O_4$ supercapacitor. Journal of the Electrochemical Society. 2007;154:A34-A8.

[16] Raymundo-Pinero E, Kierzek K, Machnikowski J, Béguin F. Relationship between the nanoporous texture of activated carbons and their capacitance properties in different electrolytes. Carbon. 2006;44:2498-507.

[17] Futaba DN, Hata K, Yamada T, Hiraoka T, Hayamizu Y, Kakudate Y, et al. Shape-engineerable and highly densely packed single-walled carbon nanotubes and their application as super-capacitor electrodes. Nature materials. 2006;5:987.

[18] Zhang LL, Zhou R, Zhao X. Graphene-based materials as supercapacitor electrodes. Journal of Materials Chemistry. 2010;20:5983-92.

[19] Stoller MD, Park S, Zhu Y, An J, Ruoff RS. Graphene-based ultracapacitors. Nano letters. 2008;8:3498-502.

[20] Wang Y, Shi Z, Huang Y, Ma Y, Wang C, Chen M, et al. Supercapacitor devices based on graphene materials. The Journal of Physical Chemistry C. 2009;113:13103-7.

[21] Zhao B, Liu P, Jiang Y, Pan D, Tao H, Song J, et al. Supercapacitor performances of thermally reduced graphene oxide. Journal of power sources. 2012;198:423-7.

[22] Ghosh S, Inganäs O. Conducting polymer hydrogels as 3D electrodes: applications for supercapacitors. Advanced Materials. 1999;11:1214-8.

[23] Liu T, Finn L, Yu M, Wang H, Zhai T, Lu X, et al. Polyaniline and polypyrrole pseudocapacitor electrodes with excellent cycling stability. Nano letters. 2014;14:2522-7.

[24] Augustyn V, Simon P, Dunn B. Pseudocapacitive oxide materials for high-rate electrochemical energy storage. Energy & Environmental Science. 2014;7:1597-614.

[25] Xia X, Tu J, Zhang Y, Wang X, Gu C, Zhao X-b, et al. High-quality metal oxide core/shell nanowire arrays on conductive substrates for electrochemical energy storage. ACS nano. 2012;6:5531-8.

[26] Chen L-F, Huang Z-H, Liang H-W, Yao W-T, Yu Z-Y, Yu S-H. Flexible all-solid-state high-power supercapacitor fabricated with nitrogen-doped carbon nanofiber electrode material derived from bacterial cellulose. Energy & Environmental Science. 2013;6:3331-8.

[27] Qu Q, Shi Y, Tian S, Chen Y, Wu Y, Holze R. A new cheap asymmetric aqueous supercapacitor: Activated carbon//$NaMnO_2$. Journal of Power Sources. 2009;194:1222-5.

[28] Bichi M, Anyata B. Industrial waste pollution in the Kano River Basin. Environmental management and health. 1999;10:112-6.

[29] Victor PA. Pollution: Economy and environment: Routledge; 2017.

[30] Igoni AH, Ayotamuno M, Eze C, Ogaji S, Probert S. Designs of anaerobic digesters for producing biogas from municipal solid-waste. Applied energy. 2008;85:430-8.

[31] Hoornweg D, Bhada-Tata P. What a waste: a global review of solid waste management. 2012.

[32] Zurbrugg C. Urban solid waste management in low-income countries of Asia how to cope with the garbage crisis. Presented for: Scientific Committee on Problems of the Environment (SCOPE) Urban Solid Waste Management Review Session, Durban, South Africa. 2002:1-13.

[33] Abioye AM, Ani FN. Recent development in the production of activated carbon electrodes from agricultural waste biomass for supercapacitors: a review. Renewable and sustainable energy reviews. 2015;52:1282-93.

[34] Ismanto AE, Wang S, Soetaredjo FE, Ismadji S. Preparation of capacitor's electrode from cassava peel waste. Bioresource technology. 2010;101:3534-40.

[35] Rufford TE, Hulicova-Jurcakova D, Zhu Z, Lu GQ. Nanoporous carbon electrode from waste coffee beans for high performance supercapacitors. Electrochemistry Communications. 2008;10:1594-7.

[36] Rufford TE, Hulicova-Jurcakova D, Khosla K, Zhu Z, Lu GQ. Microstructure and electrochemical double-layer capacitance of carbon electrodes prepared by zinc chloride activation of sugar cane bagasse. Journal of Power Sources. 2010;195:912-8.

[37] Wahid M, Puthusseri D, Phase D, Ogale S. Enhanced capacitance retention in a supercapacitor made of carbon from sugarcane bagasse by hydrothermal pretreatment. Energy & Fuels. 2014;28:4233-40.

[38] He X, Ling P, Yu M, Wang X, Zhang X, Zheng M. Rice husk-derived porous carbons with high capacitance by $ZnCl_2$ activation for supercapacitors. Electrochimica Acta. 2013;105:635-41.

[39] Gao Y, Li L, Jin Y, Wang Y, Yuan C, Wei Y, et al. Porous carbon made from rice husk as electrode material for electrochemical double layer capacitor. Applied Energy. 2015;153:41-7.

[40] Li X, Xing W, Zhuo S, Zhou J, Li F, Qiao S-Z, et al. Preparation of capacitor's electrode from sunflower seed shell. Bioresource technology. 2011;102:1118-23.

[41] Nabais JMV, Nunes P, Carrott PJ, Carrott MMLR, García AM, Díaz-Díez M. Production of activated carbons from coffee endocarp by $CO_2$ and steam activation. Fuel Processing Technology. 2008;89:262-8.

[42] Xu B, Chen Y, Wei G, Cao G, Zhang H, Yang Y. Activated carbon with high capacitance prepared by NaOH activation for supercapacitors. Materials Chemistry and Physics. 2010;124:504-9.

[43] Taer E, Deraman M, Talib I, Awitdrus A, Hashmi S, Umar A. Preparation of a highly porous binderless activated carbon monolith from rubber wood sawdust by a multi-step activation process for application in supercapacitors. Int J Electrochem Sci. 2011;6:3301-15.

[44] Farma R, Deraman M, Awitdrus A, Talib I, Taer E, Basri N, et al. Preparation of highly porous binderless activated carbon electrodes from fibres of oil palm empty fruit bunches for application in supercapacitors. Bioresource technology. 2013;132:254-61.

[45] Elmouwahidi A, Zapata-Benabithe Z, Carrasco-Marín F, Moreno-Castilla C. Activated carbons from KOH-activation of argan (Argania spinosa) seed shells as supercapacitor electrodes. Bioresource technology. 2012;111:185-90.

[46] Li L, Dong S, Chen X, Han P, Xu H, Yao J, et al. A renewable bamboo carbon/polyaniline composite for a high-performance supercapacitor electrode material. Journal of Solid State Electrochemistry. 2012;16:877-82.

[47] Chang B, Guo Y, Li Y, Yang B. Hierarchical porous carbon derived from recycled waste filter paper as high-performance supercapacitor electrodes. RSC Advances. 2015;5:72019-27.

[48] Zhi M, Yang F, Meng F, Li M, Manivannan A, Wu N. Effects of pore structure on performance of an activated-carbon supercapacitor electrode recycled from scrap waste tires. ACS Sustainable Chemistry & Engineering. 2014;2:1592-8.

[49] Konikkara N, Kennedy LJ, Vijaya JJ. Preparation and characterization of hierarchical porous carbons derived from solid leather waste for supercapacitor applications. Journal of hazardous materials. 2016;318:173-85.

[50] Fu C, Grant PS. Toward low-cost grid scale energy storage: supercapacitors based on up-cycled industrial mill scale waste. ACS Sustainable Chemistry & Engineering. 2015;3:2831-8.

[51] Lopez E, Soto B, Arias M, Nunez A, Rubinos D, Barral M. Adsorbent properties of red mud and its use for wastewater treatment. Water research. 1998;32:1314-22.

[52] Power G, Gräfe M, Klauber C. Bauxite residue issues: I. Current management, disposal and storage practices. Hydrometallurgy. 2011;108:33-45.

[53] Ruyters S, Mertens J, Vassilieva E, Dehandschutter B, Poffijn A, Smolders E. The red mud accident in Ajka (Hungary): plant toxicity and trace metal bioavailability in red mud contaminated soil. Environmental science & technology. 2011;45:1616-22.

[54] Çengeloğlu Y, Kır E, Ersöz M. Removal of fluoride from aqueous solution by using red mud. Separation and Purification Technology. 2002;28:81-6.

[55] Cengeloglu Y, Tor A, Ersoz M, Arslan G. Removal of nitrate from aqueous solution by using red mud. Separation and Purification Technology. 2006;51:374-8.

[56] Wang S, Boyjoo Y, Choueib A, Zhu Z. Removal of dyes from aqueous solution using fly ash and red mud. Water research. 2005;39:129-38.

[57] Altundoğan HS, Altundoğan S, TuÈmen F, Bildik M. Arsenic removal from aqueous solutions by adsorption on red mud. Waste Management. 2000;20:761-7.

[58] Namasivayam C, Arasi D. Removal of congo red from wastewater by adsorption onto waste red mud. Chemosphere. 1997;34:401-17.

[59] Ribeiro DV, Labrincha JA, Morelli MR. Potential use of natural red mud as pozzolan for Portland cement. Materials research. 2011;14:60-6.

[60] Qin S, Wu B. Reducing the radiation dose of red mud to environmentally acceptable levels as an example of novel ceramic materials. Green Chemistry. 2011;13:2423-7.

[61] Balakrishnan M, Batra V, Hargreaves J, Monaghan A, Pulford I, Rico J, et al. Hydrogen production from methane in the presence of red mud–making mud magnetic. Green Chemistry. 2009;11:42-7.

[62] Legodi M, De Waal D. The preparation of magnetite, goethite, hematite and maghemite of pigment quality from mill scale iron waste. Dyes and Pigments. 2007;74:161-8.

[63] Raghavender A, Hong NH, Lee KJ, Jung M-H, Skoko Z, Vasilevskiy M, et al. Nano-ilmenite FeTiO3: Synthesis and characterization. Journal of magnetism and magnetic materials. 2013;331:129-32.

[64] De La Pierre M, Carteret C, Maschio L, André E, Orlando R, Dovesi R. The Raman spectrum of CaCO3 polymorphs calcite and aragonite: a combined experimental and computational study. The Journal of Chemical Physics. 2014;140:164509.

[65] Bhattacharya G, Sas S, Wadhwa S, Mathur A, McLaughlin J, Roy SS. Aloe vera assisted facile green synthesis of reduced graphene oxide for electrochemical and dye removal applications. RSC Advances. 2017;7:26680-8.

[66] Song Q, Chiu C, Chan S. Effects of ball milling on the physical and electrochemical characteristics of nickel hydroxide powder. Journal of applied electrochemistry. 2006;36:97-103.

[67] Nath A, Jiten C, Singh KC. Influence of ball milling parameters on the particle size of barium titanate nanocrystalline powders. Physica B: Condensed Matter. 2010;405:430-4.

[68] Kutuk S. Influence of milling parameters on particle size of ulexite material. Powder Technology. 2016;301:421-8.

[69] Lin Y, Wang X, Qian G, Watkins JJ. Additive-driven self-assembly of well-ordered mesoporous carbon/iron oxide nanoparticle composites for supercapacitors. Chemistry of Materials. 2014;26:2128-37.

[70] Nagarajan N, Zhitomirsky I. Cathodic electrosynthesis of iron oxide films for electrochemical supercapacitors. Journal of Applied Electrochemistry. 2006;36:1399-405.

[71] Wu N-L, Wang S-Y, Han C-Y, Wu D-S, Shiue L-R. Electrochemical capacitor of magnetite in aqueous electrolytes. Journal of Power Sources. 2003;113:173-8.

[72] Bhattacharya G, Kandasamy G, Soin N, Upadhyay RK, Deshmukh S, Maity D, et al. Novel π-conjugated iron oxide/reduced graphene oxide nanocomposites for high performance electrochemical supercapacitors. RSC Advances. 2017;7:327-35.

[73] Ray A, Roy A, Bhattacharjee S, Jana S, Ghosh CK, Sinha C, et al. Correlation between the dielectric and electrochemical properties of $TiO_2$-$V_2O_5$ nanocomposite for energy storage application. Electrochimica Acta. 2018.

[74] Majumdar D, Baugh N, Bhattacharya SK. Ultrasound assisted formation of reduced graphene oxide-copper (II) oxide nanocomposite for energy storage applications. Colloids and Surfaces A: Physicochemical and Engineering Aspects. 2017;512:158-70.

[75] Sankar KV, Selvan RK, Meyrick D. Electrochemical performances of $CoFe_2O_4$ nanoparticles and a rGO based asymmetric supercapacitor. RSC Advances. 2015;5:99959-67.

[76] Sathiya M, Prakash A, Ramesha K, Tarascon JM, Shukla A. $V_2O_5$-anchored carbon nanotubes for enhanced electrochemical energy storage. Journal of the American Chemical Society. 2011;133:16291-9.

[77] Upadhyay KK, Altomare M, Eugénio S, Schmuki P, Silva TM, Montemor MF. On the supercapacitive behaviour of anodic porous $WO_3$-based negative electrodes. Electrochimica Acta. 2017;232:192-201.

[78] Huang C, Zhang J, Young NP, Snaith HJ, Grant PS. Solid-state supercapacitors with rationally designed heterogeneous electrodes fabricated by large area spray processing for wearable energy storage applications. Scientific reports. 2016;6:25684.

[79] Shan D, Yang J, Liu W, Yan J, Fan Z. Biomass-derived three-dimensional honeycomb-like hierarchical structured carbon for ultrahigh energy density asymmetric supercapacitors. Journal of Materials Chemistry A. 2016;4:13589-602.

[80] Senthilkumar B, Sankar KV, Vasylechko L, Lee Y-S, Selvan RK. Synthesis and electrochemical performances of maricite-$NaMPO_4$ (M= Ni, Co, Mn) electrodes for hybrid supercapacitors. RSC Advances. 2014;4:53192-200.

[81] Sankar KV, Surendran S, Pandi K, Allin A, Nithya V, Lee Y, et al. Studies on the electrochemical intercalation/de-intercalation mechanism of $NiMn_2O_4$ for high stable pseudocapacitor electrodes. Rsc Advances. 2015;5:27649-56.

[82] Yu G, Hu L, Liu N, Wang H, Vosgueritchian M, Yang Y, et al. Enhancing the supercapacitor performance of graphene/$MnO_2$ nanostructured electrodes by conductive wrapping. Nano letters. 2011;11:4438-42.

[83] Choi BG, Yang M, Hong WH, Choi JW, Huh YS. 3D macroporous graphene frameworks for supercapacitors with high energy and power densities. ACS nano. 2012;6:4020-8.

[84] Chen G-F, Liu Z-Q, Lin J-M, Li N, Su Y-Z. Hierarchical polypyrrole based composites for high performance asymmetric supercapacitors. Journal of Power Sources. 2015;283:484-93.

[85] Jafri RI, Mishra AK, Ramaprabhu S. Polyaniline–$MnO_2$ nanotube hybrid nanocomposite as supercapacitor electrode material in acidic electrolyte. Journal of Materials Chemistry. 2011;21:17601-5.

[86] Lee JW, Hall AS, Kim J-D, Mallouk TE. A facile and template-free hydrothermal synthesis of $Mn_3O_4$ nanorods on graphene sheets for supercapacitor electrodes with long cycle stability. Chemistry of Materials. 2012;24:1158-64.

[87] Li H-Q, Wang Y-G, Wang C-X, Xia Y-Y. A competitive candidate material for aqueous supercapacitors: High surface-area graphite. Journal of Power Sources. 2008;185:1557-62.

[88] Xu H, Hu Z, Lu A, Hu Y, Li L, Yang Y, et al. Synthesis and super capacitance of goethite/reduced graphene oxide for supercapacitors. Materials Chemistry and Physics. 2013;141:310-7.

[89] Wu W, He Q, Jiang C. Magnetic iron oxide nanoparticles: synthesis and surface functionalization strategies. Nanoscale research letters. 2008;3:397.

[90] Liu L, Lang J, Zhang P, Hu B, Yan X. Facile synthesis of Fe2O3 nano-dots@ nitrogen-doped graphene for supercapacitor electrode with ultralong cycle life in KOH electrolyte. ACS applied materials & interfaces. 2016;8:9335-44.

[91] Zhao C, Zheng W, Wang X, Zhang H, Cui X, Wang H. Ultrahigh capacitive performance from both $Co(OH)_2$/graphene electrode and $K_3Fe(CN)_6$ electrolyte. Scientific reports. 2013;3:2986.

[92] Ra E, Raymundo-Piñero E, Lee Y, Béguin F. High power supercapacitors using polyacrylonitrile-based carbon nanofiber paper. Carbon. 2009;47:2984-92.

[93] Tajik S, Dubal DP, Gomez-Romero P, Yadegari A, Rashidi A, Nasernejad B, et al. Nanostructured mixed transition metal oxides for high performance asymmetric supercapacitors: Facile synthetic strategy. International Journal of Hydrogen Energy. 2017;42:12384-95.

[94] Liu C, Li C, Ahmed K, Wang W, Lee I, Zaera F, et al. Scalable, binderless, and carbonless hierarchical Ni nanodendrite foam decorated with hydrous ruthenium dioxide for 1.6 V symmetric supercapacitors. Advanced Materials Interfaces. 2016;3.

[95] Macdonald JR, Barsoukov E. Impedance spectroscopy: theory, experiment, and applications. History. 2005;1.

[96] Zhang D, Zhang X, Chen Y, Yu P, Wang C, Ma Y. Enhanced capacitance and rate capability of graphene/polypyrrole composite as electrode material for supercapacitors. Journal of Power Sources. 2011;196:5990-6.

[97] Bhattacharya G, Mathur A, Pal S, McLaughlin J, Roy SS. Equivalent Circuit Models and Analysis of Electrochemical Impedance Spectra of Caffeine Solutions and Beverages. Int J Electrochem Sci. 2016;11:6370-86.

[98] Bisquert J, Garcia-Belmonte G, Bueno P, Longo E, Bulhoes L. Impedance of constant phase element (CPE)-blocked diffusion in film electrodes. Journal of Electroanalytical Chemistry. 1998;452:229-34.

[99] Bhattacharya G, Sankaran KJ, Srivastava SB, Thomas JP, Deshmukh S, Pobedinskas P, et al. Probing the flat band potential and effective electronic carrier density in vertically aligned nitrogen doped diamond nanorods via electrochemical method. Electrochimica Acta. 2017;246:68-74.

[100] Xiang C, Li M, Zhi M, Manivannan A, Wu N. A reduced graphene oxide/$Co_3O_4$ composite for supercapacitor electrode. Journal of Power Sources. 2013;226:65-70.

**Figures**

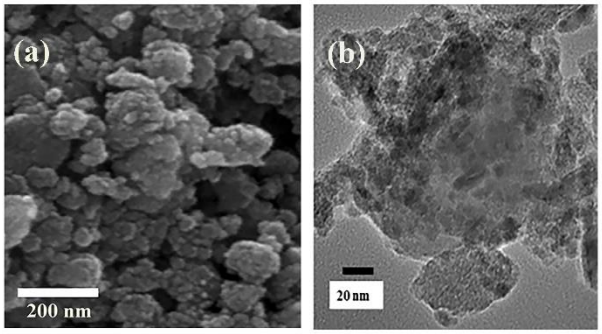


Fig.1 (a) FESEM image, 1 (b) TEM image 1(c) XRD pattern and 1 (d) Raman spectroscopy measurement for RM-0.

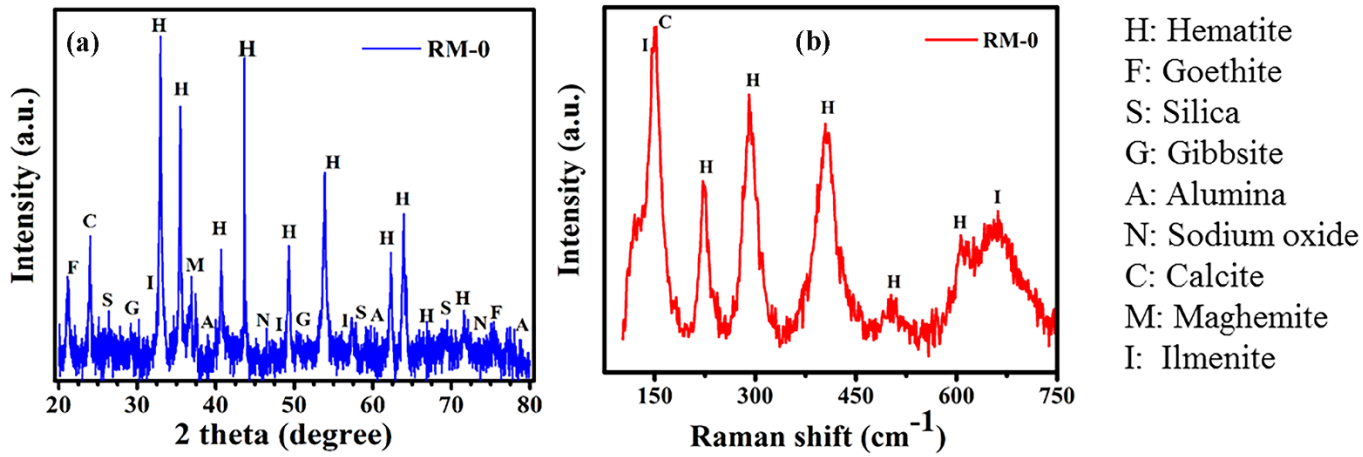


Fig.2 (a) XRD pattern and 2 (b) Raman spectroscopy measurement for RM-0.

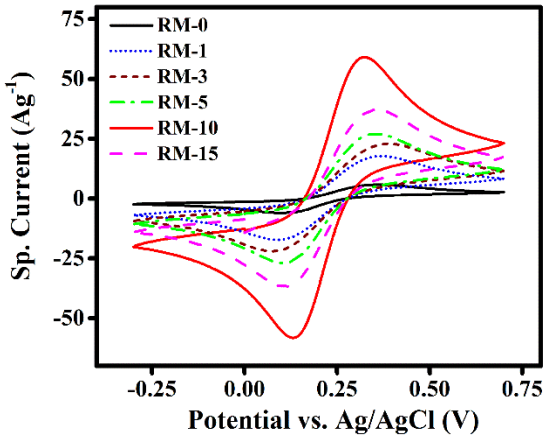


Fig. 3. Cyclic voltammogram of RM-0, RM-1, RM-3, RM-5, RM-10, and RM-15 modified GCE in the solution of 0.1 M KCl containing 5mM $[Fe(CN)_6]^{3-/4-}$ with a scan rate 50 mV $s^{-1}$.

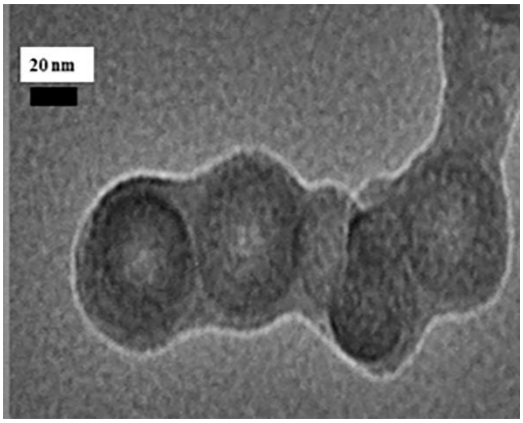


Fig. 4. TEM image of RM-10 nanoparticle.

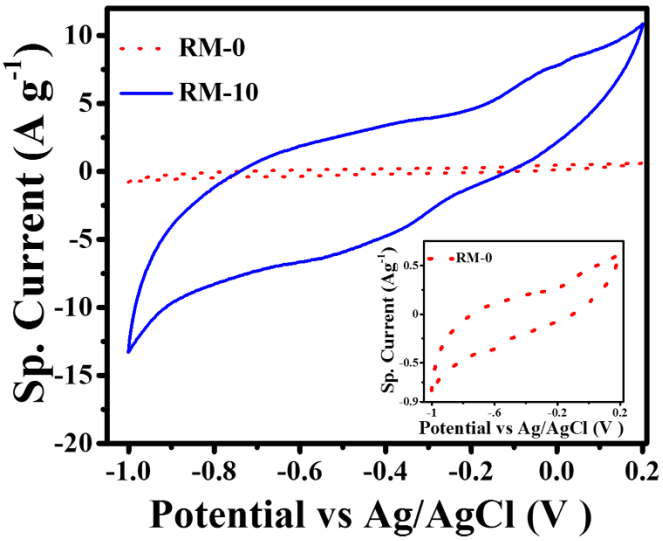


Fig. 5. Cyclic voltammogram response of RM-0 and RM-10 nanoparticle modified GCE in 6 M KOH solution with a scan rate of 10 mV $s^{-1}$. Inset shows the cyclic voltammogram response of RM-0 modified GCE in similar test conditions.

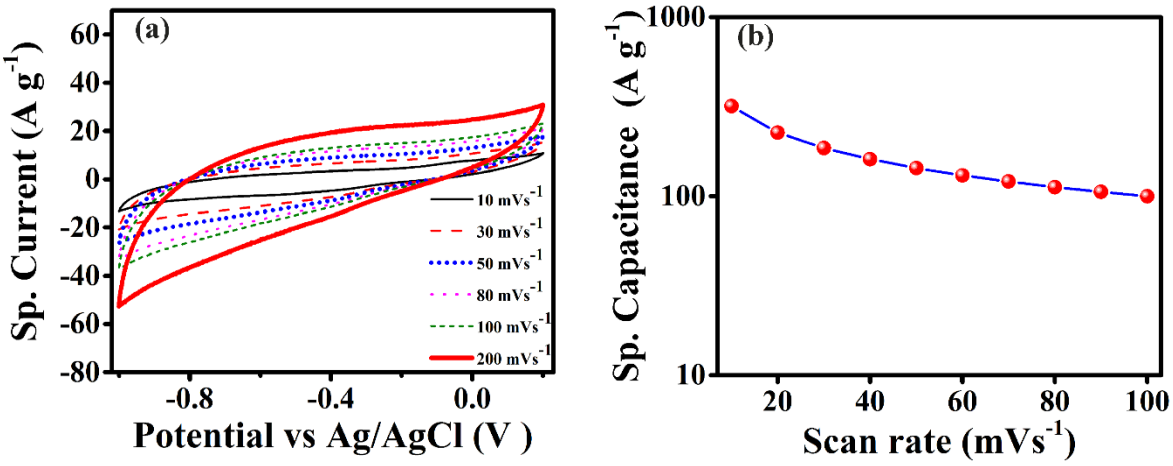


Fig. 6. (a) Cyclic voltammogram of RM-10 nanoparticle in 6 M KOH solution in different scan rate. (b) is the variation of sp. capacitance with scan rate for RM-10 nanoparticles in 6 M KOH aqueous solution.

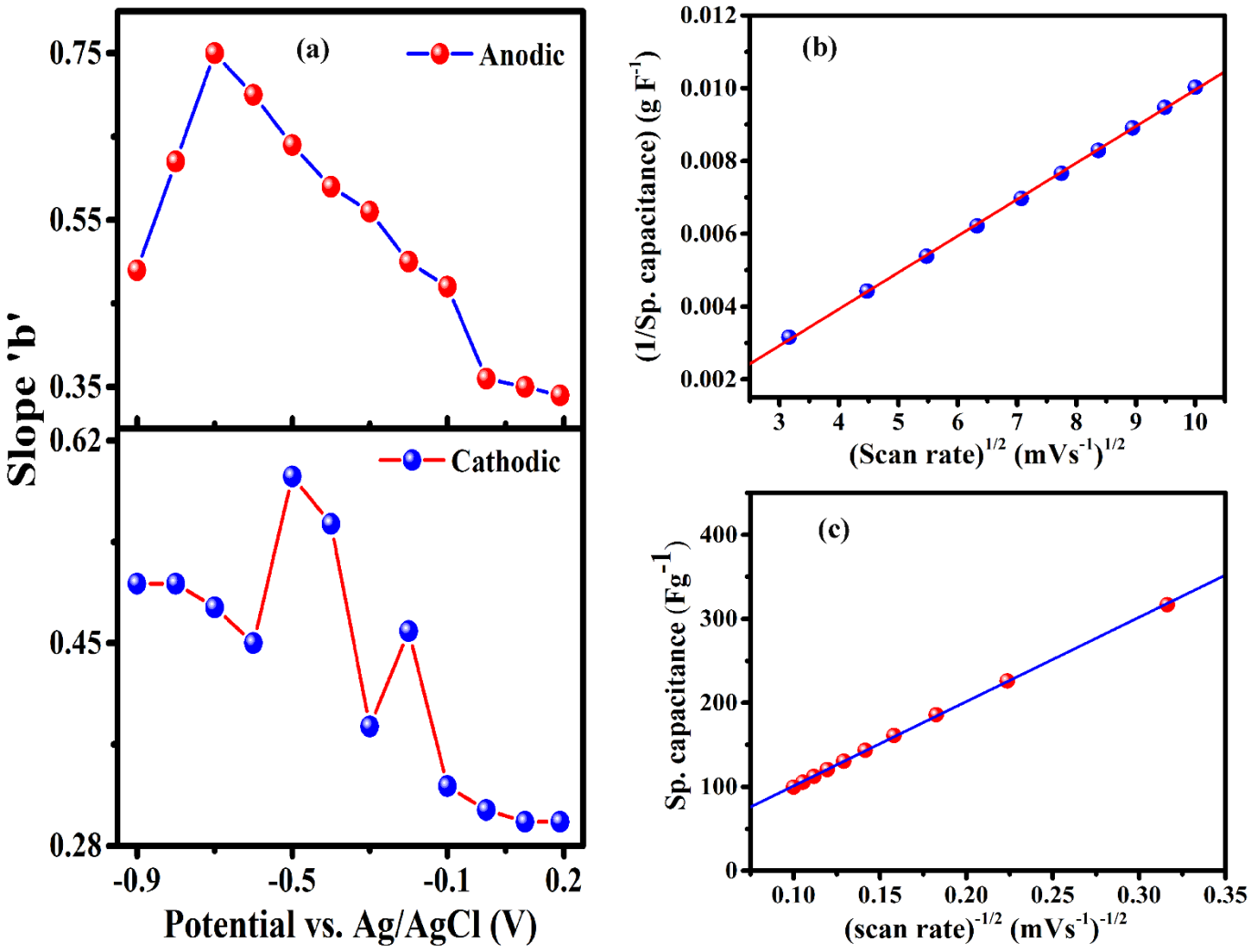


Fig. 7. (a) Dependence of slope "b" (derived from linear fitting of log $i$ vs. log $v$) as a function of cell potential and Trasatti's method for RM-10 modified electrode for (b) inverse sp. capacitance as a function of square root of scan rate and (c) sp. capacitance as a function of inverse of scan rate.

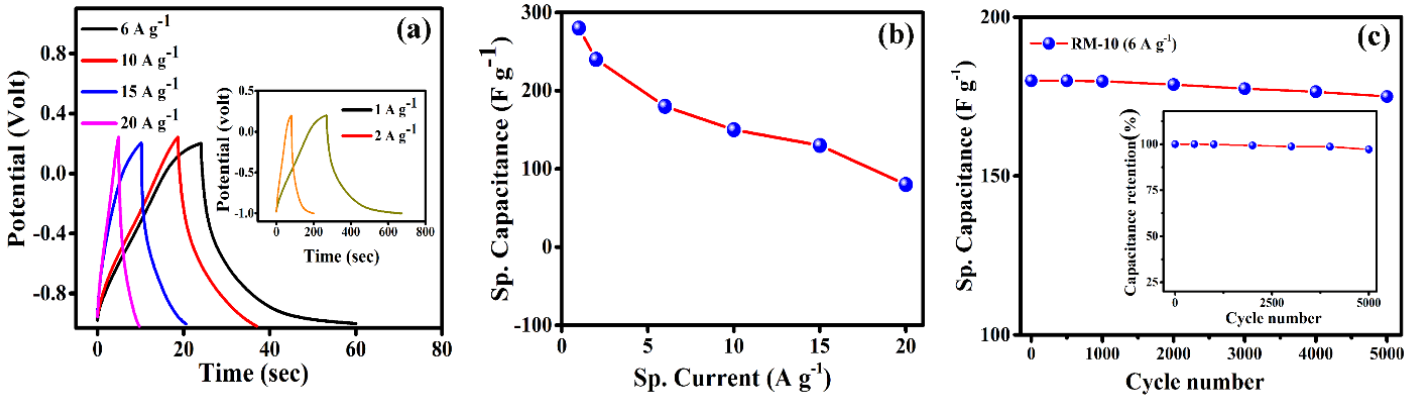


Fig. 8. (a) Galvanostatic charge/discharge curve for gravimetric capacitance of RM-10 nanoparticles in 6 M KOH aqueous solution at different sp. current (1 $Ag^{-1}$, 2 $Ag^{-1}$, 6 $Ag^{-1}$, 10 $Ag^{-1}$, 15 $Ag^{-1}$, 20 $Ag^{-1}$). (b) Variation of sp. capacitance with specific current for RM-10. (c) The cycling performance of RM-10 nanoparticles in 6 M KOH solution at sp. current 6 $Ag^{-1}$ (up to 5000 cycle). Inset of Fig. 7 (c) exhibits the percentage of capacitance retention as a function of charge-discharge cycle (up to 5000 cycles).

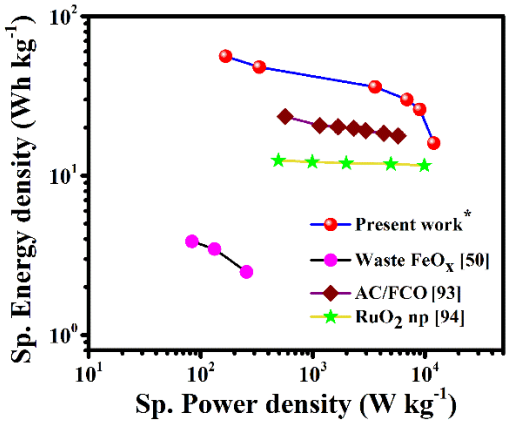


Fig. 9. Comapritive Ragone plot showing energy density and power density relationship of a few supercapcitor materials: Industrial Mill Scale Waste (waste $FeO_x$) [50] , AC/FCO nanocomposites [93], ruthenium oxide nanoparticle ($RuO_2$ np) in a two-electrode system [94], and RM-10 nanoparticles (present work)*.

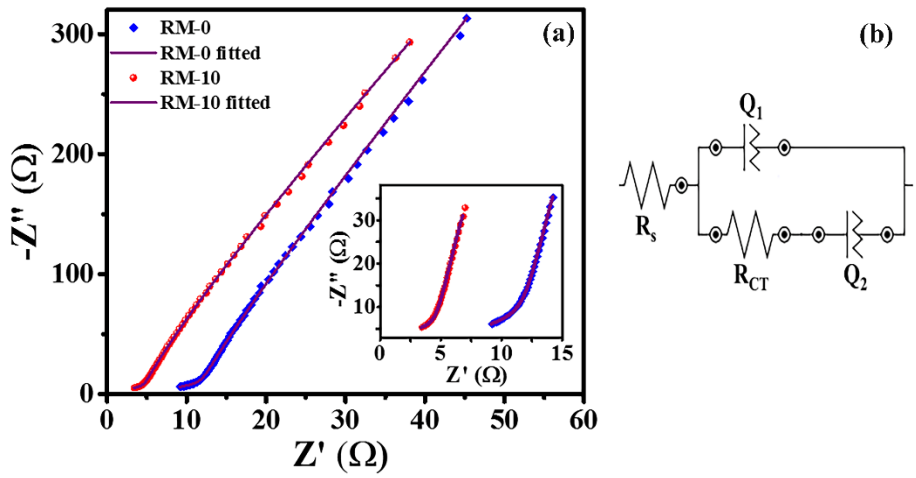


Fig. 10. (a) Nyquist plot of experimental and fitted impedance data for RM-0 (blue diamond) and RM-10 nanoparticles (red dot), the violet line corresponds to fitted data. Inset of Fig. 10 (a) depicts the zoomed view of impedance data at high-frequency region. (b) Corresponds to the model equivalent electrical circuit.

Table 1 WDXRF data of RM-0 samples.

| **Constituents** | **% (w/w)** |
|---|---|
| Iron oxide | ~55 |
| Aluminum oxide | ~15 |
| Silica | ~7 |
| Sodium oxide | ~5 |
| Titanium oxide | ~4 |
| Calcium oxide | ~3 |
| Others | ~11 |

Table 2. Experimental results of cyclic voltammetry measurements for RM-0, RM-1, RM-3, RM-5, RM-10, and RM-15 modified GCE.

| Sample | Anodic peak potential ($E_a^0$) (mV) | Cathodic peak potential ($E_a^0$) (mV) | Separation potential ($\Delta E_{dif}$) (mV) | Coulombic efficiency (η%) | Half-cell potential ($E_{1/2}^0$) (mV) |
|---|---|---|---|---|---|
| Un-milled | 361 | 103 | 258 | 96 | 232 |
| RM-1 | 371 | 090 | 281 | 97 | 230 |
| RM-3 | 386 | 073 | 313 | 97 | 229 |
| RM-5 | 352 | 105 | 247 | 98 | 228 |
| RM-10 | 325 | 129 | 196 | 98 | 227 |
| RM-15 | 383 | 078 | 305 | 97 | 230 |

Table 3. Different component of fitted parameters obtained from equivalent model electrical circuit fitting from Nyquist plot of impedance spectroscopy

| Sample | $R_S$ (Ω) | $R_{CT}$ (Ω) | $Q_1$ (μmho) | $Q_2$ (μmho) | $\chi^2$ |
|---|---|---|---|---|---|
| RM-0 | 9.1 | 17.3 | 4.0;0.9 | 8.7;0.8 | 0.001 |
| RM-10 | 3.4 | 11.2 | 5.6;0.9 | 9.1;0.8 | 0.002 |